

AUTHOR QUERIES

AUTHOR PLEASE ANSWER ALL QUERIES

PLEASE NOTE: We cannot accept new source files as corrections for your article. If possible, please annotate the PDF proof we have sent you with your corrections and upload it via the Author Gateway. Alternatively, you may send us your corrections in list format. You may also upload revised graphics via the Author Gateway.

AQ:1 = Author: Please confirm or add details for any funding or financial support for the research of this article.

AQ:2 = Please confirm whether the current affiliation of all the authors are correct as set.

AQ:3 = Please provide the department name for the current affiliation of the authors Stefano Salvatori, M. C. Rossi, and G. Conte from the universities Università degli Studi Niccolò Cusano and Università degli Studi Roma Tre.

AQ:4 = Please provide the publisher name and publisher location for Ref. [15].

AQ:5 = Please provide the accessed date for Ref. [28].

AQ:6 = Please provide the department name for Ref. [42].

Diamond Detector With Laser-Formed Buried Graphitic Electrodes: Micron-Scale Mapping of Stress and Charge Collection Efficiency

Stefano Salvatori, *Member, IEEE*, Maria Cristina Rossi, Gennaro Conte, Taras Kononenko, Maxim Komlenok, Andrey Khomich, Victor Ralchenko, Vitaly Konov, G. Provatas, and M. Jaksic

Abstract—The paper reports the micron-scale investigation of an all-carbon detector based on synthetic single crystal CVD-diamond having an array of cylindrical graphitic buried-contacts, about 20 μm in diameter each, connected at the front side by superficial graphitic strips. To induce diamond-to-graphite transformation on both detector surface and bulk volume, direct-laser-writing technique was used. Laser-treatment parameters and cell shape have been chosen to minimize the overlapping of laser-induced stressed volumes. Optical microscopy with crossed polarizers highlighted the presence of an optical anisotropy of the treated material surrounding the embedded graphitized columns, and non-uniform stress in the buried zones being confirmed with a confocal Raman spectroscopy mapping. Dark current-voltage characterization highlights the presence of a field-assisted detrapping transport mainly related to highly-stresses regions surrounding buried columns, as well as superficial graphitized strips edges, where electric field strength is more intense, too. Notwithstanding the strain and electronic-active defects, the detector demonstrated a good charge collection produced by 3.0 and 4.5 MeV protons impinging the diamond, as well as those generated by MeV β -particles emitted by ^{90}Sr source. Indeed, the mapping of charge collection efficiency with Ion Beam Induced Charge technique displayed that only a few micrometers thick radial region surrounding graphitic electrodes has a reduced efficiency, while most of the device volume preserves good detection properties with a charge collection efficiency around 90% at 60 V of biasing. Moreover, a charge collection efficiency of 96% was estimated under MeV electrons irradiation, indicating the good detection activity along the buried columns depth.

Index Terms—3D detectors, β -particles, graphitic pillars, IBC, protons, sc-CVD diamond.

Manuscript received July 12, 2019; accepted August 22, 2019. This work was supported in part by the Russian Ministry of Education and Science under Project 3.2608.2017/4.6, and in part by the Measurements at RBI have had the support of project AIDA-2020, under Grant 654168. The associate editor coordinating the review of this article and approving it for publication was Dr. Giuseppe Barillaro. (*Corresponding author: Stefano Salvatori.*)

S. Salvatori is with the Università degli Studi Niccolò Cusano, 00166 Rome, Italy (e-mail: stefano.salvatori@unicusano.it).

M. C. Rossi and G. Conte are with the Università degli Studi Roma Tre, 00146 Rome, Italy (e-mail: mariacristina.rossi@uniroma3.it; gconte@fis.uniroma3.it).

T. Kononenko, M. Komlenok, A. Khomich, V. Ralchenko, and V. Konov are with the A. M. Prokhorov General Physics Institute, Russian Academy of Sciences, 119991 Moscow, Russia (e-mail: taras.kononenko@nsc.gpi.ru; komlenok@nsc.gpi.ru; antares-610@yandex.ru; vg_ralchenko@mail.ru; vik@nsc.gpi.ru).

G. Provatas and M. Jaksic are with the Ruder Boskovic Institute, 10000 Zagreb, Croatia (e-mail: georgios.provatas@irb.hr; jaksic@irb.hr).

Digital Object Identifier 10.1109/JSEN.2019.2939618

I. INTRODUCTION

SILICON and germanium have been considered for many years the elective semiconductor materials for radiation and particle detectors fabrication. However, such tetravalent semiconductors depict a low tolerance to radiation damage and devices are less stable either in harsh conditions or under high-energy particle fluences when compared to diamond based detectors [1], [2]. Although diamond is considered as one of the best radiation-tolerant material, yet the diamond detectors show a certain degradation in terms of their detectivity upon operation under very high radiation fluences [3]. To overcome such a detrimental effect, several research groups implemented in diamond three-dimensional contact structures (an array of conductive wires embedded in bulk of the crystal) similar to those proposed for Si and GaAs based detectors [4] aimed at improving the Charge Collection Efficiency (CCE) of generated carriers. The use of such a 3D-design leads to several advantages in comparison with conventional planar electrode system, due to a possible drastic reduction of the distance between contacts: a shorter drift path of generated carriers assures a lower probability of charge trapping, guaranteeing good response even after long irradiation periods; higher electric field strengths can be achieved at lower values of the applied voltage. For diamond, buried contacts can be realized by means of either focused ion beams (also named Deep Ion Beam Lithography, DIBL) [5]–[7] or pulsed-laser treatments [8]. Those two techniques are adopted to induce a local transformation of insulating diamond into conductive graphite, hence device contact realization, also acting as distributed electrodes within the bulk material and/or on diamond surface.

The laser-induced local transformation of diamond into graphite represents a powerful tool used for the development 3D-contacts devices [9]–[13], all-carbon detectors [14]–[15], graphite resistors on diamond [16] (opening the way to redesign position sensitive devices based on distributed resistive superficial contacts [17]), as well as the realization of complex three-dimensional geometries [18]. Several research groups reported detailed investigations on their experimental process conditions [19]–[21], mainly studied to: increase the buried contact aspect-ratio (length over diameter) in order to decrease contacts' distance for the same detector active volume; assure a good buried-contact conductivity by optimizing laser-treatment parameters (power-density, scan velocity,



repetition rate) experimenting with either nanosecond, picosecond or femtosecond pulsed laser sources. However, graphitic paths are strongly process-dependent and a proper choice of laser-treatment parameters is fundamental for the realization of high quality contacts in device fabrication. For example, on a micrometer scale, a buried laser-generated graphitic column is far from an ideal cylinder and its geometry looks like a kind of a tree with thin branches spreading out not only along the laser beam direction, but also fanning out from the central body of the column, with the sp^3 to sp^2 ratio strongly dependent on the laser parameters [19], [22]. Lagomarsino *et al.* [22] reported a significant difference in morphology and electrical conductance of the buried graphitic structures fabricated by nanosecond- and femtosecond-pulsed laser radiation, with a more defective layers formed around the ns-columns. The stress [21]–[24] and defects, such as 3H defect (carbon interstitial) [25], appear around the graphitic pillars, and this should have a direct impact on local electronic properties of diamond. Sotillo *et al.* [24] applied polarized confocal Raman spectroscopy to study the origin of stress-induced waveguides in diamond, produced by femtosecond laser writing. They mapped the stress and the refractive index in a gap between adjacent buried graphitic wires arranged in close proximity to each other, on a scale of the order of $10\ \mu\text{m}$, and revealed a co-existence of tensile and compressive stress in different orientations. Salter *et al.* [26] studied the internal structure of fs-laser induced graphitic wires using TEM and electron energy loss spectroscopy and revealed multiple micro-cracks and nano-clusters of sp^2 bonded carbon embedded into sp^3 bonded diamond matrix. Ashikkalieva *et al.* [19] applied scanning spreading resistance microscopy to investigate spatial arrangement of sp^2 bonded nano-sheets forming conductive network inside wires. Forcolin *et al.* [21] used the proton microbeam to map local charge collection efficiency (CCE) with Ion Beam Induced Charge (IBIC) technique for fs-laser induced buried graphitic electrodes array. However, as the stress field was not quantified, no direct comparison of the stress and CCE maps for diamond around the electrodes, was documented.

In the present work we realized an array of buried graphitic columns in a single crystal CVD-diamond slab by means of femtosecond infrared laser, and analyzed on micron-scale the spatial distributions of stress and local charge collection efficiency of the pillared device, in the vicinity and between the graphitic electrodes, in order to establish a correlation between the damage (stress) level of the material and its electronic properties and detection capability. Graphitized superficial strips and pads, obtained applying a similar laser-treatment apparatus with ArF source, were used to define the overall detector contact geometry. Aiming at preserve the good electronic quality of the pristine diamond sample, in comparison to other investigated cell-shapes [9], [13], [27], the laser-formed buried contacts geometry of the detector was designed to minimize the overlapping between stressed regions originated by the laser-treatment itself, which mainly propagates along the $\{111\}$ crystal direction [19].

To investigate the presence of lattice defects like those already evidenced in previous devices [25], as well as strained

regions surrounding the pillar itself, we used microRaman analysis and dark field polarized optical microscopy. Ion Beam Induced Charge (IBIC) imaging with 3 and 4.5 MeV protons micro-beam was used to estimate the detection performance of the device, whereas high-energy β -particles emitted by a ^{90}Sr source were used to evaluate the charge collection efficiency along the detector thickness defined by the buried-pillars depth. Current-voltage measurements have been also used to investigate the effects of stress and defects induced by laser-treatment on the detector dark conductivity highlighting the presence of a field-assisted detrapping process in the charge carriers transport mechanism, which dominates at higher applied voltages.

II. EXPERIMENTAL DETAILS

A. Material and Detector Fabrication

A single crystal (100)-oriented “detector grade” CVD diamond $3 \times 3\ \text{mm}^2$ plate from Element Six™ with nitrogen and boron impurity content lower than 5 ppb and 1 ppb, respectively, as claimed by the producer [28], was used in this work. Using standard mechanical procedures, all surfaces of the plate were mechanically polished for final dimensions around $3 \times 3 \times 0.47\ \text{mm}^3$. (The four lateral faces were polished allowing visual inspection during the subsequent laser-process graphitization for buried-pillars fabrication.) To remove polishing residuals, the sample was then dipped in hot chromic acid solution followed by aqua regia, finally rinsed in hot DI water and in isopropanol.

For laser treatment, a computer controlled three-axis translation stage was used to hold the diamond plate precisely moved with respect to the laser beam focal point (position tolerance and repeatability better than $\pm 10\ \mu\text{m}$). A femtosecond VaryDisc50 laser (Dausinger + Giesen GmbH), operated at 1030 nm, with 400 fs of pulse duration and 200 kHz of pulse-repetition-rate, was applied for diamond-to-graphite local transformation [29]. Graphitized regions formation during the laser process was observed by means of a CCD camera coupled to a $\times 20$ microscope objective located perpendicularly to the laser beam direction.

Both the laser-pulse energy and the scan speed represent fundamental parameters for a proper device fabrication. The former was set at about $0.5\ \mu\text{J}$ and graphitic columns were induced by moving the sample along the beam direction at a constant speed of $50\ \mu\text{m/s}$. Resulting pillars were $20\ \mu\text{m}$ in diameter having a regular shape along the scan direction. As shown in Fig. 1(a), we adopted the same buried contacts geometry depicted in [29], composed by an array of “elementary cells” with dimensions $x = 150\ \mu\text{m}$ and $y = 300\ \mu\text{m}$. Compared to that used in ref. [30], a buried columns distance d around $170\ \mu\text{m}$ was preferred to maintain an adequate drift distance of charge carriers at few tens of Volts of applied bias. The rectangular face-centered cell (partially resembling a hexagonal shape [27]) adopted for the device would assure a minimized overlapping of laser-induced stressed regions mainly localized within the $\{111\}$ planes [19], [31], although this appears particularly important for relatively low d distance in micrometer range.

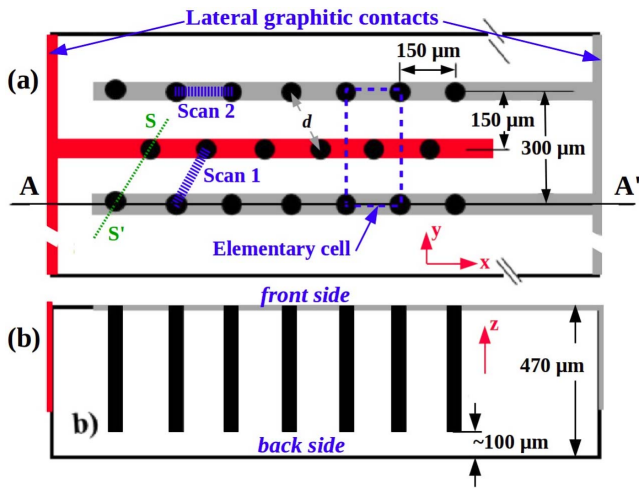


Fig. 1. Layout of the 3D-contacts detector: (a) front view of a part on the surface with graphite strips connecting buried columns. d represents the contact distance between two polarized nearest neighbor pillars. “Scan #” illustrates the directions in Raman analysis. Dotted rectangle represents the area identifying a detector “elementary-cell”; (b) cross-sectional (A-A’) view of the buried-contacts structure with end $100 \mu\text{m}$ apart the sample back side.

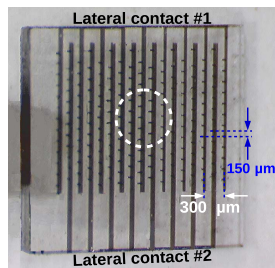


Fig. 2. Micrograph of the diamond detector (top view). Dotted circle depicts the detector area where approximately impinges the collimated β -particles beam (see text for details).

Each buried graphitic contact, about $370 \mu\text{m}$ long (in depth, see Fig. 1(b)), was produced in a single laser-irradiation step along the $[001]$ crystal direction. Columns height within the bulk, maintained $100 \mu\text{m}$ lower than diamond sample thickness, assured the presence of an insulating layer at the back of the device. In addition, compared to previous works [29], [30], laser-process adopted in the present work allowed to fabricate well-defined buried columns with a relatively low tolerance of $\pm 2\%$ in height.

The produced graphitic columns then were connected by superficial interdigitated graphitic strips on the polished sample front side, $\sim 50 \mu\text{m}$ wide, $\sim 10 \mu\text{m}$ thick, and $150 \mu\text{m}$ apart, formed with an excimer ArF laser ($\lambda = 193 \text{ nm}$). The strips were obtained by 25% overlapping of $50 \times 50 \mu\text{m}^2$ square spots with uniform laser fluence of 5 J/cm^2 . By current-voltage measurements of such superficial graphite strips (by means of a Keithley 6517A), we evaluated a resistivity around $0.16 \pm 0.02 \Omega \text{ cm}$, whereas a value around $0.5 \Omega \text{ cm}$ is estimated for buried columns [19]. Finally, to simplify external device connections, two lateral graphitized $2.5 \times 0.35 \text{ mm}^2$ rectangular pads were realized on two opposite $3 \times 0.47 \text{ mm}^2$ lateral faces (see Fig. 1) by means of the mentioned excimer laser apparatus. Fig. 2 shows the photograph of the realized detector.

Single component cyan-acrylic liquid glue was used to fix the device to a single-face Printed Circuit Board (PCB) having two copper traces “soldered” to the lateral graphitic contacts by means of silver paste. The PCB, used for device connection to the front-end and signal acquisition electronics, as well as detector biasing, allowed the irradiation also on the back side of the detector thanks to the presence of a 2 mm hole centered to the diamond die.

B. Optical Microscopy and Raman Spectroscopy

A Nikon Eclipse 50LPol microscope equipped with crossed polarizer and analyzer (black field) and a Nikon Ds-Fi1 color camera were used to investigate the optical anisotropy distribution induced by buried columns fabrication. The focal plane of a $4 \times / 0.13$ achromatic objective was maintained on the front sample surface, whereas the polarization axis was initially set parallel to the superficial graphitic strips, *i.e.* to the $\langle 110 \rangle$ crystal orientation.

For Raman analysis, a Jobin-Yvon LabRam HR800 spectrometer in a confocal configuration with spatial resolution of about $1 \mu\text{m}$, at an excitation wavelength of 473 nm , was used. The laser beam was focused either on the sample front surface or within the bulk, and the scattered light was collected in a back-scattering geometry using an Olympus microscope objective ($100 \times$, N.A. = 0.90). The spectrometer calibration, in the same conditions used for diamond sample characterization, was performed using the 1st order Raman line of a high quality type IIa natural diamond, $\nu_{D0} = 1332.5 \text{ cm}^{-1}$ with a FWHM of 1.6 cm^{-1} , used as reference.

C. Device Characterization Under MeV Electrons

Beta particles, emitted from ^{90}Sr source (1 MBq, QSA Global, code SIFB13505, item 22/2006) which have a maximum energy of 2.28 MeV , have been used to measure the detector average charge collection over the bulk material. The ^{90}Sr source was hosted inside a 25 mm long brass cylinder with an aperture of 0.4 mm in diameter and 5 mm in depth. In such a condition, the output electron beam resulted quite well collimated with a relatively small divergence: β -particles are emitted within a solid angle around $5 \times 10^{-3} \text{ sr}$. A natural diamond ADII-3 (UralAlmazInvest) fast detector (time resolution better than 1 ns) was used as trigger device and positioned 10 mm apart from the brass cylinder and positioned 10 mm apart from the brass cylinder and its front diaphragm ($\varnothing = 1.5 \text{ mm}$) was aligned to the cited solid angle of ^{90}Sr emission. The CVD-diamond Detector Under Test (DUT) was then positioned in the middle between the β -source and the ADII-3 trigger and the center of its active detection area was aligned within the mentioned emission solid angle. In such a condition, β -particles mainly impinge on about 0.5 mm^2 of the detector active area (see dotted circle in Fig. 2). The adopted setup assured that high energy electrons emitted by ^{90}Sr source have to deposit enough energy in the ADII-3 detector to be accepted as an event by the acquisition system. Both DUT and trigger signals were preamplified by using two fast rise-time and low-noise hybrid Charge Sensitive Amplifiers (CSA), CAEN A1422H-F2 (45 mV/MeV in Si).

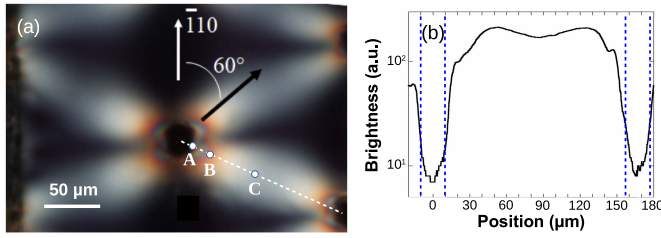


Fig. 3. (a). Cross-polarizer optical microscopy image: graphite strips parallel to the polarization axis. Bright areas around the pillars highlight different degree of stress here evidenced as optical anisotropy. A, B, and C points indicate significant positions where Raman spectra were acquired (see text). (b) Brightness profile along the dashed white line in (a) connecting two neighboring electrodes. Vertical dotted lines show the pillars extension.

269 A CAEN N6724a two-channels digitizer, 14 bit, 100 MS/s and
 270 500 mV_{pp} of dynamic range, was used for data collection and
 271 analysis using the CAEN DPP-PHA digital pulse processing
 272 software. The time acquisition window between the two chan-
 273 nels was set to 10 ns. The performed amplitude calibration
 274 procedure is described elsewhere [29]. For device voltage
 275 biasing, a CAEN N1471A power supply was used. Finally,
 276 the trigger threshold during acquisitions was set to 0.2 fC,
 277 greater than the Gaussian noise amplitude evaluated with
 278 measurement in free-running mode (external trigger disabled).

279 D. IBIC Characterization With MeV Protons

280 We performed IBIC analysis with protons at Ruder
 281 Boskovic Institute in Zagreb using a Van-de-Graaff tandem
 282 accelerator [32]. The energy of the scanning micro-beam
 283 (focus smaller than 2 μm), was set at 3.0 and 4.5 MeV. The
 284 spatial distribution of the ionization charge, evaluated with
 285 SRIM code [33], indicates that, for the mentioned energies,
 286 protons stopping power in diamond is around 48 and 97 μm,
 287 respectively, so that they are completely absorbed within
 288 the detector volume. The readout chain consisted of a CSA
 289 (ORTEC 142A) followed by a shaping amplifier (ORTEC 570)
 290 with a shaping time of 2.0 μs. A dedicated beam scanning
 291 and data acquisition system displayed the signal values on
 292 128 × 128 pixels images, reading the amplitude of the charge
 293 signal with a trigger threshold regulated to 10,000 electrons.
 294 A silicon barrier detector and a copper grid on the beam path
 295 was used to calibrate the readout chain by assuming an e-h pair
 296 production energy of 3.62 eV for silicon [34] while 13.0 eV
 297 was used to evaluate the pair production in diamond [35].

298 III. RESULTS AND DISCUSSION

299 A. Optical Microscopy Analysis

300 Optical microscopy images were acquired in a dark-field
 301 condition. The image of Fig. 3(a) clearly shows the presence of
 302 wide bright regions distributed around a buried graphitic col-
 303 umn (visible as a black dot of about 20 μm in diameter). These
 304 regions, extended for 50-80 μm from the pillar, highlight the
 305 presence of stress induced in the pristine crystal by volume
 306 expansion of the material converted to graphitic pillar. The
 307 maximum strain is concentrated along lines connecting nearest
 308 neighbor pillars, so the material compression is not isotropic,

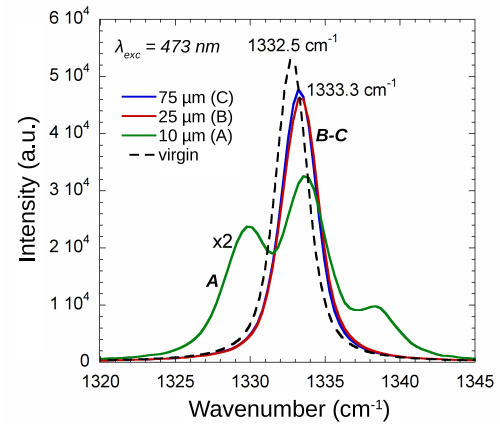


Fig. 4. Raman spectra at three different points: close the laser-treated zone (A and B), and in the middle between two buried pillars (C). A, B, and C refer to the points depicted in Fig. 3(a). Dotted curve refers to Raman spectrum of pristine diamond sample.

309 resulting in birefringence of the solid. Although the number
 310 of nearest neighbor pairs of buried columns is 6 (4 located at
 311 the cell corners and 2 belong to the same graphitic strip, see
 312 Fig. 1), Fig. 3(a) displays only 4 strain “lines” coming from the
 313 pillars forming the cell’s corner: hidden vertical plumes in the
 314 figure are oriented along the forbidden polarization direction
 315 ((110) crystal orientation), and masked by superficial graphitic
 316 strips, too. In a smaller-scale of a few microns, Fig. 3(a)
 317 also shows the presence of colored contrast in proximity of
 318 each pillar, revealing a stress change surrounding the pillar
 319 surface, as further confirmed by Raman analysis. It is worth
 320 to note the symmetry of the colored patterns, homogeneously
 321 distributed along the pillar surrounding, obtained by a proper
 322 alignment of polarizers and the diamond crystal orientation.
 323 Isochromatic fringes could be compared with Michel Lévy
 324 table [36] to estimate the local refractive index variation if
 325 the retardation value and the diamond crystal thickness are
 326 known. Conversely, to simplify the analysis, assuming the
 327 brightness of the cross-polarized image to be proportional to
 328 the stress in diamond, the images can be used as relative
 329 measure of stress [21]. The profile of the brightness along the
 330 line connecting two neighbor electrodes is shown in Fig. 3(b)
 331 on log scale, which reveals a minimum of stress in the middle
 332 between the electrodes. In addition, a sharp increase of light
 333 intensity in the regions adjacent to the buried columns is also
 334 revealed, mainly attributed to the volume expansion of the
 335 laser-formed pillar. Both the two aspects are confirmed by
 336 Raman spectroscopy analysis as illustrated in the next section.

337 B. Raman Analysis

338 Micro-Raman mapping along the line between two nearest
 339 neighbor graphitic pillars have been performed in order to gain
 340 an insight into vibrational scattering in different points close
 341 to the laser-treated volume, as well as the untreated region
 342 between two buried contacts. Significant results are summa-
 343 rized in Fig. 4 where Raman spectrum of pristine diamond is
 344 also reported for reference (dotted curve), displaying a single
 345 diamond peak at $\nu_{D0} = 1332.5 \text{ cm}^{-1}$ with a FWHM of

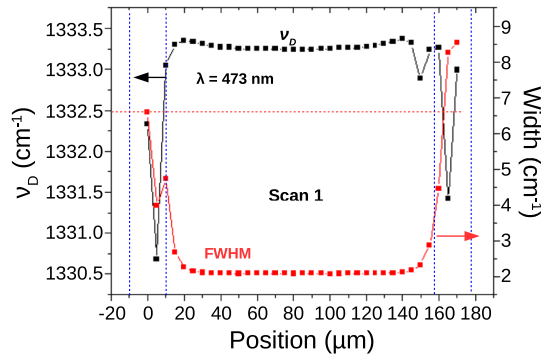


Fig. 5. Diamond peak position and FWHM evaluated from Raman spectra scanning the region between two pillars of two adjacent graphite strips (“scan 1” line in Fig. 1). The maximum upshift deviation from the reference value $\nu_{D0} = 1332.5 \text{ cm}^{-1}$, known for unstrained diamond, is lower than 1.0 cm^{-1} in the region between pillars where a constant FWHM is apparent.

346 about 2 cm^{-1} , characteristic for high quality single crystal
 347 material. In contrast, in the spectrum A, acquired $10 \mu\text{m}$
 348 apart from the pillar center (point ‘A’ of Fig. 3), diamond
 349 peak becomes asymmetric, splitting into three distinct singlet
 350 components at 1329 , 1334 , and 1339 cm^{-1} , respectively.
 351 The lower wavenumber component is found to downshifted,
 352 while the second and third ones are upshifted, suggesting a
 353 superposition of tensile and compressive stress components.
 354 Such a phenomenon reveals the presence of high anisotropic
 355 stress mainly located at the buried pillar boundary. At this
 356 time, we cannot ascertain the origin of these phonon modes
 357 and more work is needed to properly attribute the underlying
 358 mechanism of stress formation.

359 The Raman spectra acquired close to the pillar, but in the
 360 untreated volume (points ‘B’ of Fig. 3, $25 \mu\text{m}$ apart from the
 361 pillar center), and in the middle of the region between two
 362 pillars (point ‘C’, Fig. 3, $75 \mu\text{m}$ apart from the pillar center),
 363 respectively, depict a more intense diamond peak 1 cm^{-1}
 364 upshifted with respect to ν_{D0} , with unchanged FWHM of
 365 about 2 cm^{-1} . This suggests the occurrence of a structural
 366 relaxation to a compressive stress, where the cubic symmetry
 367 of diamond as well as crystalline order are preserved in the
 368 regions outside the laser-treated volumes.

369 More details on Raman spectra variations were revealed
 370 in scans performed along lines between two nearest neigh-
 371 bor pillars. Fig. 5 reports the 1st order diamond Raman
 372 peak position ν_D and FWHM value evaluated from spectra
 373 acquired every $5 \mu\text{m}$ along the bulk region between two
 374 pillars positioned on adjacent graphitic strips (“scan 1” line of
 375 Fig. 1). Analysis of the ν_D wavenumber highlights a significant
 376 change of the Raman spectra along the mapped line, which
 377 displays a strongly widened diamond peak (with FWHM up
 378 to 8.5 cm^{-1}), frequency shifted toward lower wavenumbers
 379 (up to 1.8 cm^{-1}), suggestive of a possible superposition of
 380 process related structural defects and tensile stress effects.
 381 Conversely, in the region between the two pillars, spectra
 382 highlight the existence of compressed (upshift of ν_D slightly
 383 lower than 1.0 cm^{-1}), but ordered crystal (indeed, peak
 384 width remains narrow, with $\text{FWHM} = 2.0 \text{ cm}^{-1}$). For data
 385 depicted in Fig. 5, a corresponding compressive stress around

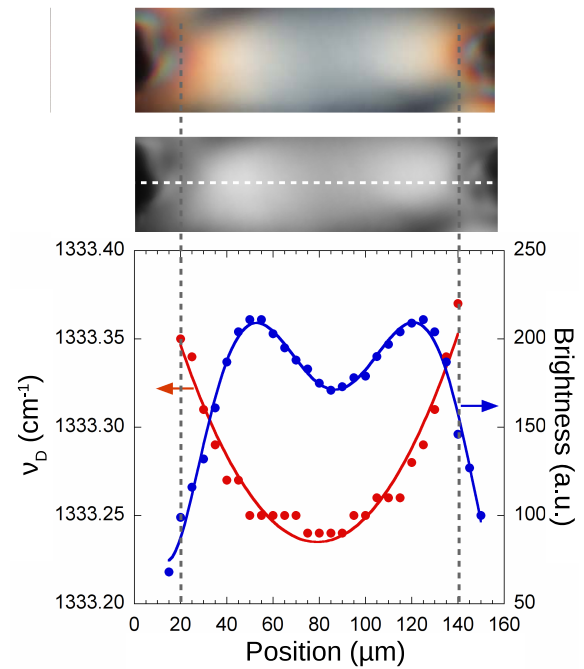


Fig. 6. Cross-polarizer optical microscopy image (top) and its corresponding images in gray tones (middle). Plot reports diamond peak position and brightness data vs. position along the dotted white line reported in the middle image. Vertical dotted lines indicate the position of maximum strain as highlighted by diamond peak shift in the Raman spectra.

386 0.38 GPa is estimated by using the relationship $\sigma = 0.38$
 387 $(\nu_D - \nu_{D0}) \text{ GPa}$ [37]. Such a result is consistent with the
 388 decrease of plumes brightness in Fig. 3, region labeled ‘C’,
 389 suggesting a lowering of crystal compression in the central
 390 region between two pillars.

391 It is worth to note that Raman peak position and image
 392 brightness in the region between the two pillars appears fairly
 393 well correlated, as shown in Fig. 6. Using a line-shape fitting
 394 procedure we were able to detect small changes ($< 0.1 \text{ cm}^{-1}$)
 395 in the diamond Raman peak position, which complement well
 396 the picture of cross-polarization optical microscopy. In the
 397 literature, the two techniques are reported as indirect stress
 398 evaluation tools [21], [38]. A behavior similar to that illus-
 399 trated in Fig. 6 has been observed using polarized micro-
 400 Raman measurements [24] between closely spaced, laser
 401 written tracks,

402 where a stress induced refractive index change is evidenced
 403 as responsible for optical guiding effect. Brightness data of
 404 Fig. 6 clearly show a strong decrease in the $\sim 20 \mu\text{m}$ wide
 405 rings surrounding each pillar. Conversely, such regions would
 406 display the highest stress as highlighted by the diamond peak
 407 shift in the Raman analysis. Brightness decrease may be
 408 a consequence of “monochromatic” light selection induced
 409 by birefringence of the crystal. However, a more detailed
 410 investigation is needed on isochromatic fringes interpretation
 411 before a self consistent analysis can be carried out.

412 Plot of Fig. 7 shows an analysis similar to that illustrated
 413 in Fig. 5, but related to the scan along two pillars of the same
 414 graphitic strips (“scan 2” line of Fig. 1). Experimental data are
 415 quite similar to the previous ones: a Raman peak downshift

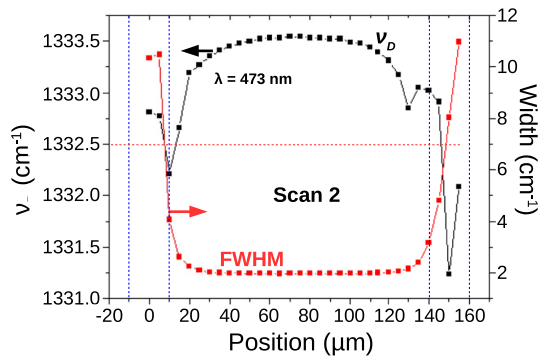


Fig. 7. Diamond peak position and FWHM evaluated from Raman spectra scanning the region between two pillars at the same superficial graphite strip (“scan 2” line in figure 1). The regions between dotted vertical lines represent the nominal buried contacts zones. Horizontal line at 1332.5 cm^{-1} corresponds to the Raman peak position for unstrained diamond.

416 and broadening detected in the pillar area and a ν_D upshift
 417 in the region between the pillars. However a slightly higher
 418 upshift (of about 1.2 cm^{-1}) is observed moving toward the
 419 region in the middle between two pillars. Such an effect can
 420 be tentatively attributed to an enhancement of compressive
 421 stress due to a lower distance between pillars of the same
 422 strip ($150 \mu\text{m}$) in comparison to that of pillars belonging two
 423 adjacent strips (about $170 \mu\text{m}$), although a small compressive
 424 contribution induced by surface graphitic strips formation
 425 cannot be ruled out. Conversely, FWHM behavior appears the
 426 same along both scanning directions. A similar investigation
 427 has been reported elsewhere [30] for a diamond detector
 428 having the same “body-centered-rectangular” 3D-cell of Fig. 1,
 429 with a pillar distance of about $280 \mu\text{m}$ and pillar diameter
 430 ranging from $30 \mu\text{m}$ (inner buried-end) to $50 \mu\text{m}$ (surface top-
 431 end). In that case, Raman analysis, performed in the region
 432 within two nearest neighbor pillars, evidenced an upshift
 433 ($\nu_D - \nu_{D0}$) of about 2.5 cm^{-1} for the diamond peak position,
 434 *i.e.* the presence of a compressive stress around 1 GPa.
 435 Comparing the two structures, it is worth to note that:
 436 *i)* a smaller pillars distance should increase crystal strain;
 437 *ii)* a smaller pillar diameter should reduce stress. The exper-
 438 imental results observed for the detector here investigated
 439 would underline that pillar diameter dominates in crystal
 440 strain. The effect induced by pillars diameter reduction is
 441 also clearly reported by Murphy *et al.* [9]. However, laser
 442 treatment speed ($50 \mu\text{m/s}$ vs. $0.5 \mu\text{m/s}$ of [30]) and fluence
 443 value differences, having a fundamental role on pillar structure
 444 formation, cannot be ruled out on the resulting stress within
 445 the bulk material and much work is in progress to investigate
 446 their influence.

447 C. Numerical Simulation of Electric Field Strength 448 and Dark Conductivity Measurements

449 A 3D structure reproducing six “elementary-cells” of the
 450 fabricated device was implemented in the finite element Flex-
 451 PDE 5.0.4 software by setting the different conductivity values
 452 of diamond ($\sigma = 5 \times 10^{-14} \text{ S/cm}$) and graphite ($\sigma = 0.2 \text{ S/cm}$)
 453 domains, as well as the dielectric permittivity (5.5 and 10 for
 454 diamond and graphite, respectively). Fig. 8 reports a view

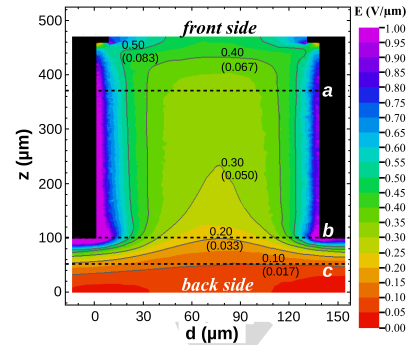


Fig. 8. Simulation results of the electric field strength distribution (at $V_a = 60 \text{ V}$) along the plane S-S’ of fig. 1(a). Equipotential perimeters are indicated to highlight the field distribution, and values corresponding at $V_a = 10 \text{ V}$ are provided between brackets. Dotted lines refer to significant depths of the device (see text).

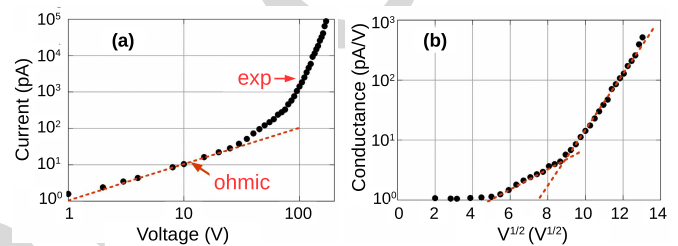


Fig. 9. (a) Current-voltage characteristics of the detector. The ohmic behavior is observed for applied bias voltages $< 30 \text{ V}$. At higher voltages, an exponential increase of current is clearly found. In (b), logarithmic plot of I/V vs. $V^{1/2}$ (Frenkel-Poole plot). Two onsets of the Frenkel-Poole regime are observed, around 25 V and 60 V of the applied bias voltage.

455 of simulated electric field distribution in the perpendicular
 456 device cross section along two pillars belonging to adjacent
 457 strips (S-S’ dotted trace of Fig. 1) for a voltage difference
 458 of 60 V. Neglecting the tip-effect distortion near the surface
 459 and at the pillars termination, a quite homogeneous field
 460 strength between the pillars is found with values ranging
 461 from $0.2 \text{ V}/\mu\text{m}$ to more than $0.5 \text{ V}/\mu\text{m}$. At the same time,
 462 electric field lines are also induced beneath the front sample
 463 side by surface graphite strips, resulting into an extension
 464 of field strength toward the central region between pillars.
 465 In the region $50 \mu\text{m}$ above the back surface, the electric field
 466 strength around $0.1\text{-}0.2 \text{ V}/\mu\text{m}$ would assure a good charge
 467 collection [39], although the contribution of carrier diffusion
 468 cannot be ruled out in untreated single-crystal diamond.

469 Laser-induced local graphitization of bulk diamond is
 470 expected to largely affect the electronic properties of the
 471 material. Fig. 9(a) shows the log-log plot of dark current-
 472 voltage characteristics acquired by means of a Keithley 6517A
 473 for the detector biased up to 200 V. For a bias voltage V_a up
 474 to few tens of Volts the device depicts an ohmic behavior,
 475 whereas it shows an exponential increase of the current
 476 amplitude at higher voltages. In agreement to a field-assisted
 477 detrapping process [40], such a behavior is compatible to the
 478 presence of defects acting as traps mainly located inside and in
 479 the vicinity of laser-formed graphitic contacts where a thick-
 480 ening of the electric field lines is also observed (see Fig. 8).

As shown in Fig. 9(b), the dark conductivity I/V displays an exponential dependence on $V^{1/2}$ for $V > 25$ V, suggesting the onset of a classical Frenkel-Pool (FP) mechanism. Conversely, for $V_a < 30$ V, conductance remains rather constant, without any evidence of non-linear effects. It is worth to observe that the FP-plot of Fig. 9(b) highlights the presence of two different onsets, to be probably attributed to the presence of two-mains shallow traps located near the edge of extended band stated. Such a phenomenon, not observed previously [30], may be attributed to: *i*) the relatively higher fluence used for buried contacts realization; *ii*) buried-columns reduced section (able to enhance the electric field strength in close proximity of the contacts at the same applied voltages); *iii*) superficial ArF-treatment able to introduce electronic-active defects mainly located at the device surface. Although results illustrated in the following sections highlight good performance of the realized device at relatively low bias voltages, further investigations are necessary to reduce electronic-active defects induced by the overall laser-process here used for device contacts fabrication.

D. Response to MeV Energy Electrons

Preliminary characterization of the detector was performed under MeV-energy electrons emitted by a ^{90}Sr source by means of the setup described in Section II.C. The device bias voltage was fixed to 10 V in order to evaluate detector performance limited by the volume defined by pillars' depth (about $370\ \mu\text{m}$). Indeed, by results of simulation of the electric field distribution, for a voltage of 10 V the electric field strength in most of the volume located in the last $100\ \mu\text{m}$ of the sample, where buried contacts are absent, is lower than $0.05\ \text{V}/\mu\text{m}$ (see values between brackets of Fig. 8). Assuming for a "detector grade" CVD-diamond sample a mobility-lifetime $\mu\tau \sim 10^{-5}\ \text{cm}^2\ \text{V}^{-1}$ [28], such an electric field would assure a charge-carrier drift around $50\ \mu\text{m}$, not enough to collect generated carriers at buried graphitic columns terminations.

The ^{90}Sr β -source emits low-energy electrons by the ^{90}Sr to ^{90}Y decay (end-point energy of 0.546 MeV), whereas the following ^{90}Y to ^{90}Zr decay produces electrons with an average energy of 939 keV and an end-point energy at about 2.28 MeV. The latter particles get across the whole diamond DUT, $470\ \mu\text{m}$ thick, releasing part of their energy and, finally, produce a signal in the ADII-3 detector used to enable the acquisition of DUT signal. Conversely, low energy β -particles, completely absorbed in diamond, are not able to produce any charge in the back trigger detector and then the signal produced in the DUT is not acquired and processed by electronics chain. As also demonstrated by Monte Carlo simulations (Casino 2.51) performed for a monochromatic electron-source of 1.1 MeV and shown in Fig. 10(a), more than 90% of impinging particles release their energy within the $470\ \mu\text{m}$ of diamond thickness. The remaining 10% get across the plate thickness, and besides, only a small fraction of them maintains the original impinging direction. Then, for the ^{90}Sr β -source we expect events recording only for particles emitted by ^{90}Y to ^{90}Zr decay, being their energy higher than the threshold of 1100 keV [41]. Events distribution

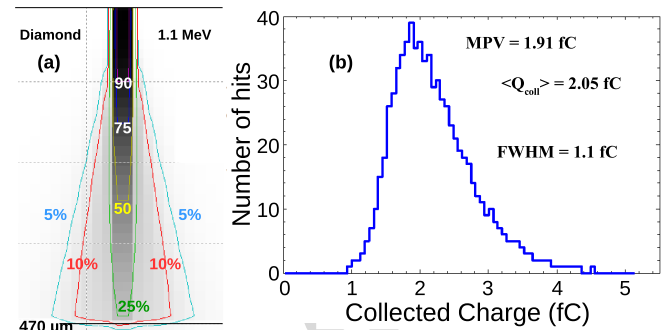


Fig. 10. (a) Cross-section view of absorbed energy in $470\ \mu\text{m}$ of diamond simulated with 1100 keV electrons (CASINO software v2.51). Contour lines show the percentage of absorbed energy contained within the line. (b) Events distribution vs. the collected charge under β -particles emitted by ^{90}Sr source.

versus the collected charge, reported in Fig. 10(b), shows a mean value $\langle Q_{coll} \rangle = 2.05 \pm 0.05\ \text{fC}$ for the collected charge, peaked at about 1.91 fC (Most Probable Value). For a rough estimation of results, let's consider such high energy β -particles as "Minimum Ionizing Particles"-like (MIPs-like). The generation rate of $36\ \text{e-h}/\mu\text{m}$ for MIPs electrons [35], [42] gives a $Q_G = 2.13\ \text{fC}$ value of generated charge carriers within the detector thickness of about $370\ \mu\text{m}$. By $CCE = \langle Q_{coll} \rangle / Q_G$ relationship, a collection efficiency around 96% is estimated, in agreement to what expected for the high-quality diamond sample used in this work ($CCE > 95\%$ [28]). Such results confirm the effectiveness of the adopted buried-columns geometry as previously predicted in [29]. In addition, compared to other solutions where either superficial metal contacts or multi-wire bonding are implemented [9],[27], [29], [30], the proposed laser direct-writing of contacts largely simplifies the fabrication of an all-carbon diamond-based device for beta-particles detection.

E. Response to MeV Energy Protons

Aimed at evaluating detector activity in the volume defined by pillars' length, as estimated by β -particles irradiation, IBIC characterization has been performed irradiating the device, biased at 60 V, either on the front or on the back surface. Indeed, with protons mainly releasing their energy around a depth of $97\ \mu\text{m}$ (4.5 MeV) or $48\ \mu\text{m}$ (3.0 MeV), IBIC analysis allowed to observe CCE in thin volumes located at the depths indicated as dotted lines in Fig. 8: for protons impinging on the detector front side, CCE mainly refers to a volume where pillars are embedded (dotted line 'a'); when back irradiation is concerned, IBIC maps refer to regions at pillars termination or within a non-contacted bulk (lines 'b' and 'c', respectively).

Fig. 11(a) reports a map acquired irradiating a $300 \times 300\ \mu\text{m}^2$ area of the front surface of the detector with 4.5 MeV protons (see inset). The acquisition mainly reflects the collection efficiency of charges generated about $100\ \mu\text{m}$ below the sample front side. The color distribution homogeneity of the image reflects wide regions (92% of the investigated area) with an almost constant CCE around 90%. Worth to observe the good collection efficiency

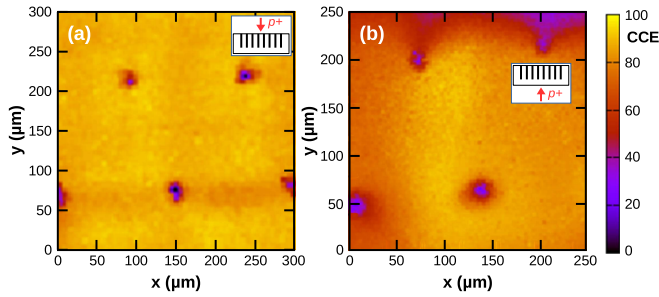


Fig. 11. (a) IBIC map of a $300 \times 300 \mu\text{m}^2$ area of the sample biased at 60 V. 4.5 MeV protons beam impinges on the top side of the detector (inset). (b) IBIC map of a $250 \times 250 \mu\text{m}^2$ area of the detector biased at 60 V. 4.5 MeV protons impinges on the back side of the device (inset).

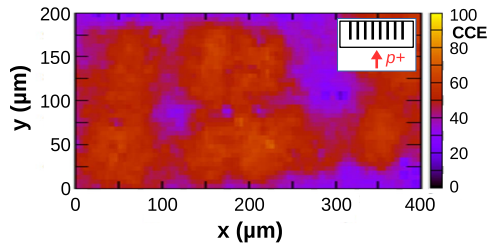


Fig. 12. IBIC map of a portion of the explored area with 3.0 MeV protons back irradiation (inset).

found in the areas where both Raman analysis and optical microscopy highlight strained regions extending for tens of microns (see Figs. 3 and 5). Buried contact positions are visible as blue-black colored dots representing a completely blind region equal to 1-2% of the total active area. At the same time a dramatic decrease of CCE, down to 60-70%, is found at about $10 \mu\text{m}$ wide pillar surroundings, where both optical microscopy and Raman spectroscopy show large stress signatures. Laser-treatment induced stress then influences CCE only close to the pillar itself, while further in the diamond bulk CCE is barely affected, as already reported [30]. This confirms the effectiveness of direct-laser-writing of diamond if compared, for example, to DIBL in which residual damages strongly affect the electronic properties of bulk material overlaying the buried-contacts structure [5].

In order to confirm that the detector active volume extends at a depth defined by pillars length, IBIC measurements were repeated irradiating the diamond detector on the back side. Fig. 11(b) shows the CCE map in a $250 \times 250 \mu\text{m}^2$ area under 4.5 MeV protons. In such a case, due to the depth of Bragg's peak of such protons, the generation of charge carriers is observed in a thin volume including the pillars terminations. Notwithstanding that the image shows the presence of wider regions of low CCE located around the pillars position, experimental results demonstrate a full activity of buried contacts. The acquisition now reflects a low homogeneity in the CCE distribution: wide diamond areas (60%) with $\text{CCE} > 70\%$ and low CCE around the pillars (in about a $20 \mu\text{m}$ domain size surrounding the pillars). Hence, almost blind-regions now extends up to 5% of the investigated area. Such a behavior probably reflects variations induced by

pillars resistivity and length able to create an electric field distortion on the volume where carriers are generated.

Finally, Fig. 12 reports a $400 \times 200 \mu\text{m}^2$ IBIC map obtained using 3.0 MeV protons, again irradiating the detector from its back side. Being $\sim 47 \mu\text{m}$ the stopping range in diamond of 3 MeV protons, back irradiation involves untreated pristine diamond. However, electric field strength is high enough in most of the region giving a CCE around 60%. On the other hand, wide areas around pillars position exhibit a lower CCE, slightly higher than 20%, addressing the possibility to collect generated carriers, but with a relatively low efficiency.

IV. CONCLUSIONS

Presently, the possibility to design detectors with a 3D-contact architecture, based on laser-induced transformation of insulating diamond into conducting graphite inside the bulk material and on the diamond surface, opens the way to fabricate diamond devices with sophisticated geometry which can easily be customized and adapted to the specific application, including position sensitive particle detectors and X-ray imaging [43]. In this work, graphitic conductive pillars fabricated in the bulk of a single crystal CVD diamond sample by femtosecond infrared laser and superficial graphitic strips by ArF excimer laser allowed the realization of an *all-carbon* detector having an interdigitated contacts structure and showing good performance under MeV energy particles irradiation. Moreover, the two lateral laser-formed graphic contacts largely simplified device mounting on a PCB holder, avoiding the need of wire bonding. Chosen laser scan speed, as well as fluence, allowed to realize well defined buried columns. Dark-conductivity measurements have been used to investigate the presence of electronic-active defects induced by laser-treatment. A Frenkel-Pool transport-mechanism is observed and tentatively attributed to traps located in regions close to contacts edges where electric field strength is more intense, too. In addition, polarized optical microscopy and confocal micro-Raman spectroscopy investigations highlight stress development and structural disorder on a micrometer scale at the pillar periphery and between the buried columns electrodes. In the pillar area the structural modification promoted by laser irradiation reveals graphitic sp^2 bonded carbon intermixed with highly defected sp^3 bonded diamond, as evidenced by a linewidth broadening and downward shifting of the diamond peak. Within the pillar surrounding the diamond peak gradually recover its characteristics of crystalline counterpart. At the same time, a compressive stress build up at the boundary with untreated diamond, owing to the volume expansion in the pillar area. Within the untreated diamond, the stress gradually relaxes towards an equilibrium value, which depend on the relative spatial distance of laser-formed buried electrodes, but leaving unaltered the crystalline quality of diamond.

Notwithstanding the presence of structural and point defects induced by diamond-to-graphite laser writing, device characterization under β -particles irradiation points out an almost full-charge collection of generated carriers along the detector contacts-thickness at a relatively low applied bias voltage.

In addition, IBIC technique was used to evaluate mapping of charge collection efficiency, showing that most of the active volume preserves good detection properties, largely decaying close to the laser-treated zones occupied by buried electrodes. For an applied bias voltage of 60 V, under 4.5 MeV protons, a CCE value around 90% is found and uniformly distributed in the regions between buried columns, where it decreases down to 70% in a 10 μm pillar surrounding. IBIC maps obtained for impinging protons on the back side of the detector demonstrate a full activity of buried contact, in agreement to what argued under β -particles irradiation.

ACKNOWLEDGMENT

The authors wish to thank the assistance of E. E. Ashkinazi and G. Della Ventura for access to optical microscopy with polarized light.

REFERENCES

- [1] E. Fretwurst *et al.*, "Recent advancements in the development of radiation hard semiconductor detectors for S-LHC," *Nucl. Instrum. Methods Phys. Res. Sect. A, Accel., Spectrometers, Detect. Associated Equip.*, vol. 552, nos. 1–2, pp. 7–19, Oct. 2005.
- [2] N. Venturi *et al.*, "Results on radiation tolerance of diamond detectors," *Nucl. Instrum. Methods Phys. Res. Sect. A, Accel., Spectrometers, Detect. Associated Equip.*, vol. 924, pp. 241–244, Apr. 2019.
- [3] D. Asner *et al.*, "Diamond pixel modules," *Nucl. Instrum. Methods Phys. Res. Sect. A, Accel., Spectrometers, Detect. Associated Equip.*, vol. 636, no. 1, pp. S125–S129, Apr. 2011.
- [4] S. I. Parker, C. J. Kenney, and J. Segal, "3D—A proposed new architecture for solid-state radiation detectors," *Nucl. Instrum. Methods Phys. Res. Sect. A, Accel., Spectrometers, Detect. Associated Equip.*, vol. 395, no. 3, pp. 328–343, Aug. 1997.
- [5] J. Forneris *et al.*, "IBIC characterization of an ion-beam-micromachined multi-electrode diamond detector," *Nucl. Instrum. Methods Phys. Res. Sect. B, Beam Interact. Mater. At.*, vol. 306, pp. 181–185, Jul. 2013.
- [6] M. De Feudis *et al.*, "Ohmic graphite-metal contacts on oxygen-terminated lightly boron-doped CVD monocrystalline diamond," *Diamond Rel. Mater.*, vol. 92, pp. 18–24, Feb. 2019.
- [7] P. Olivero *et al.*, "Focused ion beam fabrication and IBIC characterization of a diamond detector with buried electrodes," *Nucl. Instrum. Methods Phys. Res. Sect. B, Beam Interact. Mater. At.*, vol. 269, no. 20, pp. 2340–2344, Oct. 2011.
- [8] B. Caylar, M. Pomorski, and P. Bergonzo, "Laser-processed three dimensional graphitic electrodes for diamond radiation detectors," *Appl. Phys. Lett.*, vol. 103, no. 4, Jul. 2013, Art. no. 043504.
- [9] S. A. Murphy *et al.*, "Laser processing in 3D diamond detectors," *Nucl. Instrum. Methods Phys. Res. Sect. A, Accel., Spectrometers, Detect. Associated Equip.*, vol. 845, no. 1, pp. 136–138, Feb. 2017.
- [10] M. Girolami *et al.*, "Graphite distributed electrodes for diamond-based photon-enhanced thermionic emission solar cells," *Carbon*, vol. 111, pp. 48–53, Jan. 2017.
- [11] F. Bachmair *et al.*, "A 3D diamond detector for particle tracking," *Nucl. Instrum. Methods Phys. Res. Sect. A, Accel., Spectrometers, Detect. Associated Equip.*, vol. 786, pp. 97–104, Jun. 2015.
- [12] E. Alemanno *et al.*, "Laser induced nano-graphite electrical contacts on synthetic polycrystalline CVD diamond for nuclear radiation detection," *Diamond Rel. Mater.*, vol. 38, pp. 32–35, Sep. 2013.
- [13] S. Lagomarsino *et al.*, "Three-dimensional diamond detectors: Charge collection efficiency of graphitic electrodes," *Appl. Phys. Lett.*, vol. 103, no. 23, 2013, Art. no. 233507.
- [14] M. Komlenok *et al.*, "Diamond detectors with laser induced surface graphite electrodes," *Nucl. Instrum. Methods Phys. Res. Sect. A, Accel., Spectrometers, Detect. Associated Equip.*, vol. 837, pp. 136–142, Nov. 2016.
- [15] P. Oliva, S. Salvatori, G. Conte, A. P. Bolshakov, and V. G. Ralchenko, "Diamond detectors with graphite contacts," in *Advances in Sensors Review*, 5th, S. Y. Yurish Ed., 2018, ch. 2.
- [16] J. Weidner, P. Boudreaux, J. Fitz, and G. De La Grange, "Laser induced graphite resistors in synthetic diamond," *Int. J. Microcircuits Electron. Packag.*, vol. 19, no. 2, pp. 169–178, 1996.
- [17] S. Salvatori, G. Mazzeo, and G. Conte, "Voltage division position sensitive detectors based on photoconductive materials—Part I: Principle of operation," *IEEE Sensors J.*, vol. 8, no. 2, pp. 188–193, Feb. 2008.
- [18] B. Sun, P. S. Salter, and M. J. Booth, "High conductivity micro-wires in diamond following arbitrary paths," *Appl. Phys. Lett.*, vol. 105, no. 23, Nov. 2014, Art. no. 231105.
- [19] K. K. Ashikkalieva *et al.*, "Nanostructured interior of laser-induced wires in diamond," *Diamond Rel. Mater.*, vol. 91, pp. 183–189, Jan. 2019.
- [20] M. Girolami, A. Bellucci, P. Calvani, S. Orlando, V. Valentini, and D. M. Trucchi, "Raman investigation of femtosecond laser-induced graphitic columns in single-crystal diamond," *Appl. Phys. A, Solids Surf.*, vol. 117, no. 1, pp. 143–147, Oct. 2014.
- [21] G. T. Forcolin *et al.*, "Study of a 3D diamond detector with photon and proton micro-beams," *Diamond Rel. Mater.*, vol. 65, pp. 75–82, May 2016.
- [22] S. Lagomarsino *et al.*, "Electrical and Raman-imaging characterization of laser-made electrodes for 3D diamond detectors," *Diamond Rel. Mater.*, vol. 43, pp. 23–28, Mar. 2014.
- [23] S. M. Pimenov *et al.*, "Metastable carbon allotropes in picosecond-laser-modified diamond," *Appl. Phys. A, Solids Surf.*, vol. 116, no. 2, pp. 545–554, Mar. 2014.
- [24] B. Sotillo *et al.*, "Polarized micro-Raman studies of femtosecond laser written stress-induced optical waveguides in diamond," *Appl. Phys. Lett.*, vol. 112, no. 3, 2018, Art. no. 031109.
- [25] A. A. Khomich *et al.*, "Very long laser-induced graphitic pillars buried in single-crystal CVD-diamond for 3D detectors realization," *Diamond Rel. Mater.*, vol. 90, pp. 84–92, Nov. 2018.
- [26] P. S. Salter, M. J. Booth, A. Courvoisier, D. A. J. Moran, and D. A. MacLaren, "High resolution structural characterisation of laser-induced defect clusters inside diamond," *Appl. Phys. Lett.*, vol. 111, no. 8, Aug. 2017, Art. no. 081103.
- [27] M. J. Booth *et al.*, "Study of cubic and hexagonal cell geometries of a 3D diamond detector with a proton micro-beam," *Diamond Rel. Mater.*, vol. 77, pp. 137–145, Aug. 2017.
- [28] *The Element Six CVD Diamond Handbook*. [Online]. Available: https://e6cvd.com/media/wysiwyg/pdf/E6_CVD_Diamond_Handbook.pdf
- [29] G. Conte *et al.*, "Three-dimensional graphite electrodes in CVD single crystal diamond detectors: Charge collection dependence on impinging β -particles geometry," *Nucl. Instrum. Methods Phys. Res. Sect. A, Accel., Spectrometers, Detect. Associated Equip.*, vol. 799, pp. 10–16, Nov. 2015.
- [30] M. Girolami *et al.*, "Investigation with β -particles and protons of buried graphite pillars in single-crystal CVD diamond," *Diamond Rel. Mater.*, vol. 84, pp. 1–10, Apr. 2018.
- [31] T. V. Kononenko, E. V. Zavedeev, V. V. Kononenko, K. K. Ashikkalieva, and V. I. Konov, "Graphitization wave in diamond bulk induced by ultrashort laser pulses," *Appl. Phys. A, Solids Surf.*, vol. 119, no. 2, pp. 405–414, May 2015.
- [32] M. Jakšić *et al.*, "New capabilities of the Zagreb ion microbeam system," *Nucl. Instrum. Methods Phys. Res. Sect. B, Beam Interact. Mater. At.*, vol. 260, no. 1, pp. 114–118, Jul. 2007. doi: [10.1016/j.nimb.2007.01.252](https://doi.org/10.1016/j.nimb.2007.01.252).
- [33] J. F. Ziegler, M. Ziegler, and J. Biersack, "SRIM—The stopping and range of ions in matter (2010)," *Nucl. Instrum. Methods Phys. Res. Sect. B, Beam Interact. Mater. At.*, vol. 268, nos. 11–12, pp. 1818–1823, Jun. 2010. doi: [10.1016/j.nimb.2010.02.091](https://doi.org/10.1016/j.nimb.2010.02.091).
- [34] G. Knoll, *Radiation Detection and Measurement*, 4th ed. Hoboken, NJ, USA: Wiley, 2000, ch. 9.
- [35] L. S. Pan, S. Han, and D. R. Kania, *Diamond: Electronic Properties and Applications*, Norwell, MA, USA: Kluwer, 1995, ch. 10.
- [36] J. G. Delly, *The Michel-Lévy Interference Color Chart—Microscopy's Magical Color Key*. Hooke College of Applied Sciences, Westmont, IL, USA, 2003. [Online]. Available: <https://www.mccrone.com/the-michel-levy-interference-color-chart-microscopys-magical-color-key/>
- [37] A. Tardieu, F. Cansell, and J. P. Petitet, "Pressure and temperature dependence of the first-order Raman mode of diamond," *J. Appl. Phys.*, vol. 68, no. 7, pp. 3243–3245, 1998.
- [38] M. H. Grimsditch, E. Anastassakis, and M. Cardona, "Effect of uniaxial stress on the zone-center optical phonon of diamond," *Phys. Rev. B, Condens. Matter*, vol. 18, no. 2, pp. 901–904, 1978.
- [39] J. Isberg, J. Hammersberg, H. Bernhoff, D. J. Twitchen, and A. J. Whitehead, "Charge collection distance measurements in single and polycrystalline CVD diamond," *Diamond Rel. Mater.*, vol. 13, nos. 4–8, pp. 872–875, 2004.
- [40] J. Frenkel, "On pre-breakdown phenomena in insulators and electronic semi-conductors," *Phys. Rev.*, vol. 54, pp. 647–648, Oct. 1938.

- 808 [41] (2009). *Dosimeter Performance*. Accessed: Mar. 9, 2019 [Online]. Avail- 861
 809 able: <http://alignment.hep.brandeis.edu/Devices/Dosimeter/Performance.html> 862
 810 811
 812 [42] S. Zhao, "Characterization of the electrical properties of polycrystalline 863
 813 diamond films," Ph.D. dissertation, Ohio State Univ., Columbus, OH, 864
 814 USA, 1994. 865
 815 [43] M. Girolami, P. Allegrini, G. Conte, D. M. Trucchi, V. G. Ralchenko, 866
 816 and S. Salvatori, "Diamond detectors for UV and X-ray source imaging," 867
IEEE Electron Device Lett., vol. 33, no. 2, pp. 224–226, Feb. 2012. 868



817 **Stefano Salvatori** (M'00) received the Ph.D. degree 869
 818 in electronic engineering from the Università degli 870
 819 Studi Roma Tre, Rome, Italy. 871

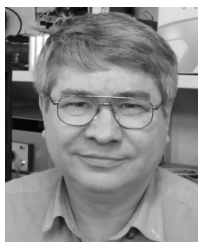
820 He is currently an Associate Professor of Elec- 872
 821 tronics with the Faculty of Engineering, Univer- 873
 822 sità degli Studi Niccolò Cusano, Rome, Italy. His 874
 823 research activity is mainly focused on diamond- 875
 824 based sensors for UV, X-ray, and particle detection, 876
 825 including processing and characterization of thin- 877
 826 film optoelectronic devices. He is primarily involved 878
 827 in the development of low-noise single- and multi- 879
 828 channel front-end electronics for low-level signal sensors. He is the Chair 880
 829 of the Technical Committee on Radiation and Particle Detectors in the Italy 881
 830 Chapter of the IEEE Sensors Council. 882



831 **Maria Cristina Rossi** was born in Rome, Italy, 883
 832 in 1962. She received the Ph.D. degree in electronic 884
 833 engineering from the Università degli Studi Roma 885
 834 "La Sapienza" in 1993. In 1994 she became a 886
 835 Research Associate with the Università degli Studi 887
 836 Roma Tre, Rome, where he became an Associate 888
 837 Professor in 2006. Her research interests include but 889
 838 are not limited to transport properties in nanostruc- 890
 839 tured semiconductors and related electronic devices. 891



840 **Gennaro (Rino) Conte** teaches physics of electronic 892
 841 and optoelectronic devices with the Università degli 893
 842 Studi Roma Tre, Rome. He has been researching 894
 843 solid-state devices for over 40 years. His interests 895
 844 have ranged from the transport properties of amor- 896
 845 phous silicon to the fabrication of surface channel 897
 846 MESFET devices on diamond. His current activity 898
 847 focuses on elementary particle detectors based on 899
 848 3D graphite-diamond structures. 900



849 **Taras Kononenko** received the M.S. degree in 901
 850 applied physics and mathematics from the Moscow 902
 851 Institute of Physics and Technology, Russia, in 1990, 903
 852 and the Ph.D. degree in laser physics from the A. 904
 853 M. Prokhorov General Physics Institute, Moscow, 905
 854 in 1996. He is currently a Senior Research Scien- 906
 855 tist with the Department of Light-induced Surface 907
 856 Phenomenon, A. M. Prokhorov General Physics 908
 857 Institute. His research interests are in the area of 909
 858 laser processing of materials, especially carbon- 910
 859 based materials like amorphous carbon films, mono-
 860 and polycrystalline diamond, and carbon fiber reinforced plastics.



861 **Maxim Komlenok** was born in Moscow, Russia, 862
 863 in 1983. He received the B.S. and M.S. degrees 864
 865 in general physics from Lomonosov Moscow State 866
 867 University Russia, in 2006, and the Ph.D. degree 868
 869 in laser physics from the A. M. Prokhorov General 870
 871 Physics Institute (GPI), RAS, Moscow, Russia, 872
 873 in 2013. 874

875 Since 2013, he has been holding a post-doctoral 876
 877 position with the Laser Induced Surface Phenom- 878
 879 ena Department, GPI RAS. He has authored more 879
 880 than 40 papers. His research interests include laser 880
 881 processing and characterization of different carbon materials (diamonds, 881
 882 nanodiamonds, diamond like carbon films, nanotubes, graphene, and graphite), 882
 883 spectroscopic diagnostics, and structure modification. 883
 884 884



875 **Andrey Khomich** received the Ph.D. degree in 875
 876 solid state physics from the A. M. Prokhorov Gen- 876
 877 eral Physics Institute, Russian Academy of Sci- 877
 878 ences, Moscow, in 2016. He is currently a Senior 878
 879 Researcher with the Radio Engineering and Elec- 879
 880 tronics Institute, Russian Academy of Sciences, 880
 881 Fryazino. His research activity is focused on the 881
 882 optical spectroscopy of carbon materials, mainly 882
 883 natural and synthetic diamonds, nanodiamonds, and 883
 884 radiation damaged diamonds. 884



885 **Victor Ralchenko** received the Ph.D. degree in 885
 886 quantum electronics from the A. M. Prokhorov Gen- 886
 887 eral Physics Institute, Russian Academy of Sciences 887
 888 (GPI RAS), Moscow, in 1989. He is currently the 888
 889 Head of the Diamond Materials Laboratory, GPI 889
 890 RAS. His research activity is mainly focused on 890
 891 CVD diamond growth and characterization, and on 891
 892 diamond applications for Raman laser, ionization 892
 893 radiation detectors, and photon emitters on color 893
 894 centers. 894



895 **Vitaly Konov** is a well-known specialist in 895
 896 synthesis, characterization, laser processing, and 896
 897 the photonic applications of novel carbon materials 897
 898 (CVD diamond, single-wall carbon nanotubes, and 898
 899 graphene). 899

900 His scientific carrier is associated with the 900
 901 A. M. Prokhorov General Physics Institute, Moscow, 901
 902 where he is currently the Director of the Natural 902
 903 Sciences Center. He is also a Professor with Moscow 903
 904 State University. Since 2000, he has been a mem- 904
 905 ber of the Russian Academy of Sciences, in 1992. 905
 906 He became a Fellow of the International Society for Optical Engineering – 906
 907 SPIE. 907

908 **G. Provatias**, photograph and biography not available at the time of 908
 909 publication. 909

910 **M. Jaksic**, photograph and biography not available at the time of publication. 910